Bull Earthquake Eng (2017) 15:1853–1880
DOI 10.1007/s10518-016-0050-1

ORIGINAL RESEARCH PAPER

Ground motion prediction equations for the Chilean subduction zone

Benjamín Idini[1] · Fabián Rojas[1,2] · Sergio Ruiz[3] · César Pastén[1]

Received: 12 April 2016 / Accepted: 10 November 2016 / Published online: 21 November 2016

Abstract The Chilean subduction zone is one of the most active in the world. Six events of magnitude greater than $M_w = 7.5$ have occurred in the last 10 years, including the 2010 $M_w = 8.8$ Maule, the 2014 $M_w = 8.2$ Iquique, and the 2015 $M_w = 8.3$ Illapel earthquakes. These events have produced a considerable dataset to study interface thrust and intraslab intermediate depth earthquakes. In this paper, we present a database of strong motion records for Chilean subduction zone earthquakes and develop a ground motion prediction equation (GMPE) for peak ground acceleration and response spectral accelerations with 5% damping ratio for periods between 0.01 and 10 s. The dynamic soil amplification effects are considered in a new empirical model based on two parameters, the predominant period of the soil (T^*) and the average shear wave velocity down to 30 m depth (V_{S30}). The spectral accelerations prediction equations at short periods are generated using 114 records of intraslab earthquakes ($M_w = 5.5$–7.8) and 369 records of interface earthquakes ($M_w = 5.5$–8.8); a reduced number of these records are used for longer periods. The proposed GMPE can predict the ground motion of large Chilean subduction earthquakes ($M_w > 8$) with no need of extrapolation from small-magnitude earthquake data. Intraslab earthquakes show a steeper attenuation slope than that of interface ones, which is consistent with other GMPE results derived from worldwide subduction zones data. Moreover, the Chilean interface earthquakes show a flatter attenuation slope relative to the Japanese ones.

Electronic supplementary material The online version of this article (doi:10.1007/s10518-016-0050-1) contains supplementary material, which is available to authorized users.

✉ Benjamín Idini
bidini@ing.uchile.cl

[1] Department of Civil Engineering, University of Chile, Av. Blanco Encalada 2002, Santiago, Chile

[2] Advanced Mining Technology Center, FCFM, University of Chile, Santiago, Chile

[3] Department of Geophysics, University of Chile, Av. Blanco Encalada 2002, Santiago, Chile

Keywords Ground motion prediction equations · Chilean subduction zone · Site effects · Response spectra

1 Introduction

Large destructive earthquakes ($M_w \geq 7.5$) occur quite frequently in subduction zones. Nowadays, it is broadly accepted the use of ground motion prediction equations (GMPEs) to assess dynamic effects on structures through seismic hazard analysis. Unfortunately, there is a lack of available ground motion records of subduction zones relative to those available for earthquakes that ocurred on other tectonic regimes (e.g. regions of shallow crustal seismicity, Bommer et al. 2010). In the previous decade, this situation denied the development of robust GMPEs for any specific subduction region, which led to undesirable extrapolation of GMPEs developed from small magnitude earthquakes to assess the seismic hazard of large earthquakes.

An approach to mitigate this shortcoming has been the development of models that combine data from many different regions and introduce corrections to account for specific regional phenomena when its needed (Youngs et al. 1997; Atkinson and Boore 2003; Abrahamson et al. 2016). A detailed review of some of these models and their databases can be found in Arango et al. (2012). Another approach has been the generation of stochastic ground motions from given earthquake scenarios (Boore 2003; Edwards and Fäh 2013; Otarola and Ruiz 2016) to close the gaps of regional databases in subduction zones. For example, Gregor et al. (2002) derived a GMPE for the Cascadia subduction zone that includes several simulated large earthquakes with $M_w \leq 9$.

Regardless of the success or failure of these approaches, the number of records increases each year in active subduction regions, which motivates the generation of new local GMPEs [e.g, McVerry et al. (2006) for New Zealand, García et al. (2005) and Arroyo et al. (2010) for Mexico, Zhao et al. (2006b) for Japan, Skarlatoudis et al. (2013) for Greece, and Lin and Lee (2008) for Taiwan]. Contreras and Boroschek (2012) is the most up-to-date GMPE for the Chilean subduction zone. Nevertheless, it has important limitations, such as it does not accounts for intraslab earthquakes, their ground motion predictions have a narrow range of spectral accelerations, it has an old-fashioned functional form that oversimplifies site effects, and their database do not include the most recent $M_w \geq 8.2$ Chilean earthquakes [e.g., the 2014 $M_w = 8.2$ Iquique (Ruiz et al. 2014; Schurr et al. 2014) and the 2015 $M_w = 8.3$ Illapel (Ruiz et al. 2016) earthquakes].

In addition to the subduction zone models, the amount of new GMPEs grows with even greater pace in other tectonic regimes (Bommer et al. 2010), which has motivated the generation of different selection criteria to prioritize their use in modern seismic hazard analysis (Scherbaum et al. 2004; Cotton et al. 2006; Bommer et al. 2010; Stewart et al. 2015). These selection criteria define some desired characteristics of modern GMPEs that guide the development of new models.

The purpose of this study is to develop a new GMPE for subduction zones from a database of large Chilean subduction earthquakes to be used in modern seismic hazard analysis. The site effect model, the signal proccessing, and the functional form are derived or selected following the requirements set in the Next Generation Attenuation Project (NGA, Power et al. 2008) to develop a new generation of GMPEs, and the selection criteria applied by the Global Earthquake Model (GEM, Di Alessandro et al. 2012b) to

recommend groups of GMPEs to be used in seismic hazard assessment at different tectonic regimes.

The use of records of large subduction Chilean earthquakes allows the derivation of a GMPE that do not requires of great magnitude extrapolation until $M_w \approx 9$ for interface earthquakes and $M_w \approx 8$ for intraslab earthquakes. Also, the use of only Chilean earthquake data allows discussing if there are regional effects on the results through the comparison of them with GMPE models derived from other regions.

This paper is divided in eight sections. Section 2 describes the Chilean earthquake database used, including the processing methodology applied to raw records. Section 3 shows the functional form used to account for path and source contributions to ground motion. Section 4 describes the methodology applied in the derivation of the empirical site effects coefficients used to account for the site contribution to ground motion. Section 5 describes the regression methodology used for the derivation of the GMPE coefficients showed in Sect. 3. Section 6 analyzes specific characteristics of the proposed GMPE and compares the ground motion predictions with the data and with other studies. Section 7 discusses the results. Finally, Sect. 8 summarizes the main novelties of the study and gives simple instructions for the user of the GMPE.

2 Chilean earthquake database

The strong motion records of Chilean earthquakes were obtained from the National Seismological Center (CSN) and from the National Accelerometer Network of the Department of Civil Engineering (RENADIC), both from the University of Chile. From the raw data, a subset of 1207 strong motion records from interface earthquakes $M_w \geq 5.5$ and intermediate depth intraslab earthquakes $M_w \geq 5$, whose 184 epicenters are shown in Fig. 1a, was selected. These two types of earthquakes are the most frequent in Chile. Due to the geometry of the Chilean subduction zone, interface earthquake ruptures are shallower than that of the intraslab earthquakes and their epicenters are generally located to the west of the intraslab earthquake ones (see Fig. 1a).

To develop the GMPE, a new subset from the complete Chilean subduction earthquakes database was selected. Firstly, we applied magnitude-dependent limits to distance in order to avoid any bias caused by the trigger threshold of accelerometers (Abrahamson et al. 2016) (see Table 1). Secondly, another group of records was removed using a signal processing criteria that is described in Sect. 2.2. As a result, the selected data subset used in the GMPE derivation consisted of 114 strong motion records of 38 intraslab earthquakes and 369 strong motion records of 65 interface earthquakes (see Table S1 in the Electronic Supplement). For intraslab earthquakes the distances ranged from 61 to 386 km, and for interface earthquakes the distances ranged from 31 to 391 km. Figure 1b, c show the GMPE data subset selected from the complete Chilean earthquake database using the magnitude-dependent limits, and whose records met the signal processing requirements described in Sect. 2.2.

2.1 Instrumentation

Figure S1 (see the Electronic Sumpplementary Material) shows the location of the 154 seismic stations used in this study. The largest densities of instruments are located in the Northern Chile (20°S) and in the Central Chile (33.5°S, near Santiago, the capital of

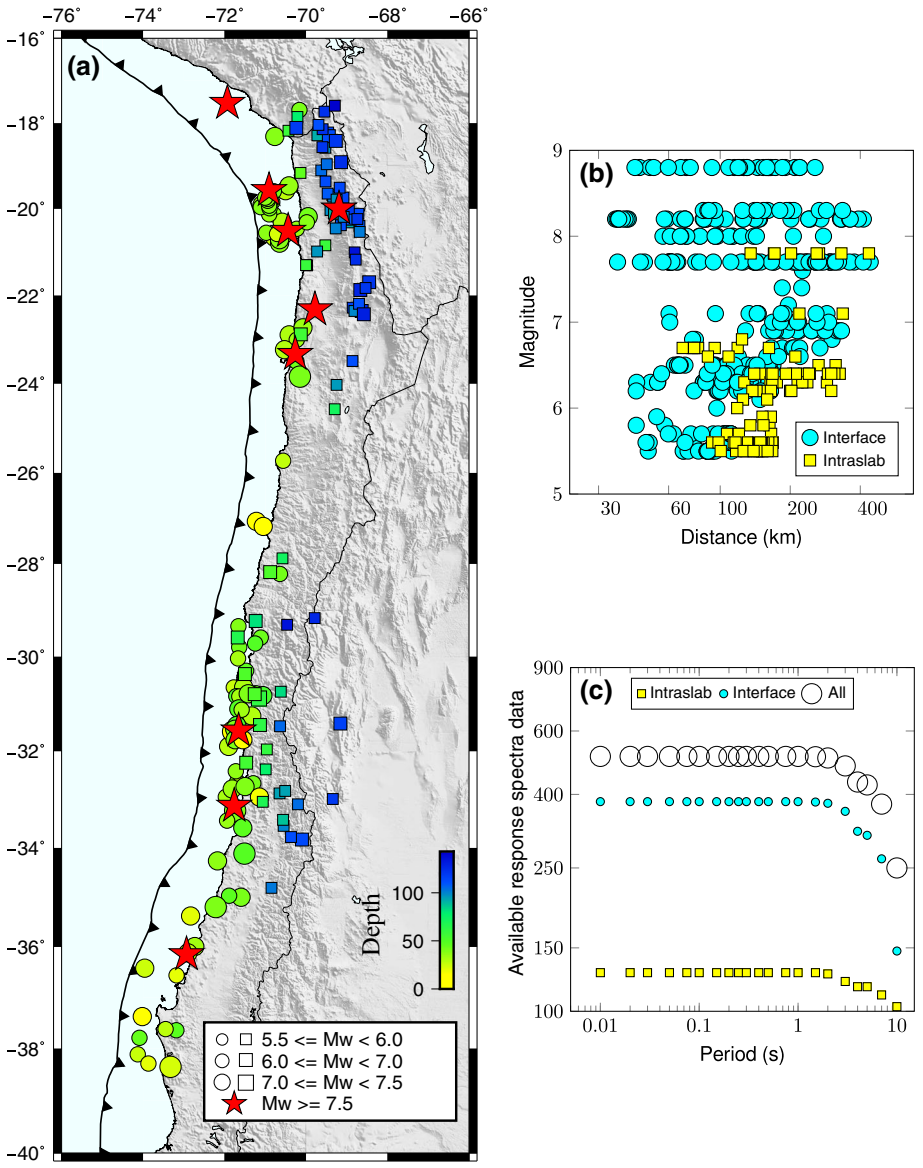

Fig. 1 The database used in this study. **a** Spacial distribution of the hypocenters. *Circles* indicate interface earthquakes and *squares* indicate intraslab earthquakes. **b** Magnitude versus distance of the data subset used in the GMPE derivation. **c** Total number of response spectra data used in the GMPE derivation at each period

Chile). The Northern Chile stations recorded the main shock and aftershocks of the 2014 Iquique earthquake (Ruiz et al. 2014), which ruptured an area close to them. The Central Chile stations partially recorded the 2010 Maule earthquake (Vigny et al. 2011), which ruptured an area from 34°S to 38°S where only a few number of accelerometers were

Table 1 Magnitude-dependent limits to distance applied in the selection of the GMPE data subset

M_w range	Intraslab R limit (km)	Interface R limit (km)
$5.5 \leq M_w \leq 6.0$	$R \leq 150$	$R \leq 100$
$6.0 < M_w \leq 6.5$	$R \leq 300$	$R \leq 150$
$6.5 < M_w \leq 7.5$	$R \leq 300$	$R \leq 300$
$M_w > 7.5$	$R \leq 400$	$R \leq 400$

located. A similar low density of instruments was located close to the rupture area of the 2015 Illapel earthquake (Ruiz et al. 2016)

Although the majority of the CSN and RENADIC networks sensors are now digital, analog sensors were common in the past and some are still in operation. For instance, all the records of the 1985 $M_w = 8.0$ Central Chile earthquake are from analog SMA-1 sensors. Also, most records of the recent $M_w = 8.8$ Maule 2010 earthquake were recorded with SMA-1 sensors or with QDR instruments, which are an upgrade of the SMA-1 sensor that incorporates an analog-to-digital converter. Earthquakes of the Northern Chile, such as the 2014 $M_w = 8.2$ Iquique and the 2015 $M_w = 8.3$ Illapel earthquake, have been recorded with modern digital instruments, such as the CMG-5 and the FBA ES-T. As a result, analog records are the 22% of the GMPE data subset, and the seismic stations with analog sensors (SMA-1 and QDR) represent the 41% of that included in the complete Chilean data base.

The films recorded by the SMA-1 sensors were digitized by RENADIC, and regardless of the digitization method, the records exhibit higher low frequency noise than records of digital sensors because of the limitations on the low frequency recording capabilities of the SMA-1 sensor and because they suffer from low frequency noise introduction generated in the digitization process (Boore and Bommer 2005). Although the QDR records do not suffer from the same low frequency noise introduction of the SMA-1 records, they have similar recording limitations at high frequencies because the fundamental frequencies of both instruments are almost the same. On the other hand, digital sensors have a better analog-to-digital converter and higher fundamental frequency than the QDR or SMA-1 instruments.

2.2 Processing of raw data

The raw data was processed using the methodology proposed by Boore and Bommer (2005), Boore (2005), Akkar and Bommer (2006), Douglas and Boore (2011), and Boore and Goulet (2014). First, a standard base line correction was applied to remove the trend. Then, a Tukey window (cosine tapper) was applied over the 5% of total length of the detrended signal to avoid Gibbs' effect in the Fourier transform. Zero padding was added to both sides of the signal with 30 s length (Boore 2005). To deal with high and low frequency noise, low-pass and high-pass fourth order Butterworth acausal filters were applied at different corner frequencies. Corner frequencies values (f_c) of high-pass filters were chosen depending on the instrument. The high-pass f_c was chosen at 0.2 Hz for analog SMA-1 instruments, at 0.1 Hz for QDR instruments, and at 0.06 Hz for other digital sensors. The longest period of the 5%-damped acceleration response spectra was chosen following the method proposed by Boore and Bommer (2005) and detailed in Akkar and Bommer (2006) that determines the period range at which the reduction of the response

spectra produced by the filter application is tolerable. Figure 1c shows the final data set used for regressions at every period. For analog and QDR records, the low-pass corner frequency was chosen at 25 Hz. For digital records, low-pass filters were required (Boore and Goulet 2014) when the Fourier amplitude spectra (FAS) showed an unusual high frequency amplitude over the natural decay of the signal amplitude with frequency. This was the case of records from sensors with natural frequencies smaller than the Nyquist frequency, which increased the FAS with resonance. In most cases of digital sensors, low-pass filtering was not needed (e.i. for the GMPE data subset, a low-pass filter was applied to the 3% of the records because of unusual high frequency content in digital records). Douglas and Boore (2011) and Boore and Goulet (2014) recommend avoiding low-pass filters when the 5%-damped acceleration response spectra depends on the low frequency content. This criterion is equivalent to:

$$\frac{FAS_{max}}{FAS_{high}} > 10 \tag{1}$$

where FAS_{max} is the peak FAS value and FAS_{high} is the FAS value at high frequencies close to the Nyquist frequency or the corner frequency of the anti-aliasing filter for digital instrument records. For analog and QDR records, FAS_{high} was taken as the FAS value at 25 Hz. If Eq. (1) was not satisfied, it implied that the record had lost important high frequency content, hence, the record was removed from the data subset. This was the case for 91 records of the complete Chilean database, which were mostly recorded by analog instruments at rock sites located close to the seismic sources.

2.3 Magnitude, distance to source, type of earthquake and depth

The moment magnitudes M_w were obtained from moment tensor solutions published in the online Global CMT Catalog (Ekström et al. 2012) and in the Centennial Earthquake Catalog (Engdahl and Villaseñor 2002). Few strong motion records of $m_b < 6$ earthquakes were excluded since the M_w is not available. Hypocenter coordinates were taken from the CSN online catalog and from the International Seismological Centre (ISC) Bulletin.

We used a hypocentral depth criterion to identify intermediate depth intraslab and deep earthquakes. In general, seismicity cross-sections of the Chilean subduction zone show that the hypocentral depths of interface earthquakes are located from 10 to 50 km approximately, the hypocentral depths of intraslab earthquakes are located from 60 to 150 km, and the hypocentral depths of deep intraslab earthquakes are located deeper than 150 km. As hypocentral depths near 55 ± 5 km led to ambiguous identification, we added an additional criterion based on the dip and strike reported in the moment tensor solution. The interface earthquakes of the Chilean subduction zone usually dip at an angle of $20° \pm 5°$ and strike at $0° \pm 20°$. The approach followed with hypocentral depths less than 50 km was to locate the position of the nearest seismogenic contact zone proposed by Hayes et al. (2012) and compare it with the position of the hypocenter. The interface Chilean earthquake hypocenters are located near to the contact zone while crustal earthquake ones are located far from it. In addition, the previous dip and strike criterion for interface earthquake identification was used assuming the same uncertainty considerations. We did not use the deep intraslab earthquake records in this study.

To evaluate the distance from the site to the seismic source, we used finite fault rupture models proposed for $M_w \geq 7.7$ interface earthquakes. The finite fault rupture models are considered as rectangular areas that represent the average slip area reported for each

earthquake by several authors. Christensen and Ruff (1986) and Mendoza et al. (1994) were used for the 1985 $M_w = 8.0$ Valparaíso earthquake, Béjar-Pizarro et al. (2010) and Peyrat et al. (2010) were used for the 2007 $M_w = 7.7$ Tocopilla earthquake, Vigny et al. (2011), Moreno et al. (2012), and Ruiz et al. (2012) were used for the 2010 $M_w = 8.8$ Maule earthquake, Ruiz et al. (2014) and Schurr et al. (2014) were used for the 2014 $M_w = 8.2$ Iquique earthquake, and Ruiz et al. (2016)was used for the 2015 $M_w = 8.3$ Illapel earthquake. In all these cases, the distance R was defined as the closest distance from the site to the finite fault rupture area. However, in the case of intraslab and $M_w < 7.7$ interface earthquakes, the distance R was taken as the distance from the site to the earthquake hypocenter.

A full list of the 5%-damped acceleration response spectra used, and the information described in this section associated to them, is shown in Table S1 in the Electronic Supplement.

3 The functional form

To select a functional form, we followed the traditional practice of breaking the response spectra into the contributions of the seismic source (F_F), the path effects between the seismic source and the site (F_D), and the local site effects (F_S) (Boore 2003). The contribution of each effect can be described by a different term and the logarithm of the response spectra is the sum of all of them,

$$\log_{10} Y = F_F(M_w, H, F_{eve}) + F_D(R, M_w, F_{eve}) + F_S \quad (2)$$

where Y is the peak ground acceleration or the acceleration response spectra for 5%-damped oscillator as a function of period in g, M_w the moment magnitude, H the hypocentral depth, F_{eve} a dummy variable that equals 0 for interface events and 1 for intraslab events, and R the source distance defined as the hypocentral distance for intraslab and $M_w < 7.7$ interface earthquakes, and as the closest distance to rupture area for $M_w \geq 7.7$ interface earthquakes.

The source contribution term F_F and the path contribution term F_D were selected using an iterative approach. A simple couple of terms were used as the starting point of the selection methodology: a linear function ($a + bM_w$) for the source contribution term and a logarithmic function ($c \log(R)$) for the distance contribution term. Additional complexity was adopted in the term definitions based on observations made to the Chilean ground motion data and the functional forms used by Atkinson and Boore (2003), Zhao et al. (2006a), and Abrahamson et al. (2016). For example, from PGA versus distance plots, a different attenuation slope for interface and intraslab earthquakes of the same magnitude was identified. As a consequence, a modifier to the geometrical spreading (g) was added as a function of the type of earthquake. Also, as the functional form of Abrahamson et al. (2016) modifies the geometrical spreading as a function of the earthquake magnitude, the PGA versus distance plots were inspected to look for evidence of this scaling effect. After a positive identification in the data, the modifier used by Abrahamson et al. (2016) was incorporated to the F_D contribution term. A similar approach was used to incorporate the saturation effect in sites close to the source. This effect and other desirable features as the consideration of ground motion saturation with magnitude, magnitude-dependent distance scaling, and the use of a anelastic attenuation term were included to the functional form following the selection criteria of Stewart et al. (2015).

Complexity was added to the terms only when a clear effect was identified in the data and it was not reproduced by the last version of the functional form. For example, no quadratic magnitude scaling effect in intraslab earthquakes was found and this effect was added only to the F_F contribution of interface earthquakes.

The selected source contribution term F_F was

$$F_F(M_w, H, F_{eve}) = c_1 + c_2 M_w + c_8(H - h_o)F_{eve} + \Delta f_M \tag{3}$$

where

$$\Delta f_M = \begin{cases} c_9 M_w^2; & F_{eve} = 0 \\ \Delta c_1 + \Delta c_2 M_w; & F_{eve} = 1 \end{cases} \tag{4}$$

and $h_o = 50$ km.

The selected path contribution term F_D was

$$F_D(R, M_w, F_{eve}) = g \log_{10}(R + R_o) + c_5 R \tag{5}$$

where

$$R_o = (1 - F_{eve})c_6 \cdot 10^{c_7[M_w - M_r]} \tag{6}$$

and

$$g = (c_3 + c_4[M_w - M_r] + \Delta c_3 F_{eve}) \tag{7}$$

$M_r = 5$ was used as a reference magnitude value. The coefficients c_i ($i = 1, 2, \ldots, 9$) and Δc_j ($j = 1, 2, 3$) are regression coefficients.

4 Empirical site effect model

The site contribution term F_S was selected by a novel approach derived from the methods used by Zhao et al. (2006a), Fukushima et al. (2007), and Di Alessandro et al. (2012a). The functional form in Eq. (2) can be written as

$$S_{hs}(T) = S_{hr}(M_w, H, F_{eve}, R; T) f_s(T) \tag{8}$$

where S_{hs} is the horizontal response spectra at a given soil site condition, S_{hr} is the horizontal response spectra at a rock site, and f_s is a spectral shape factor that describes the modification of the rock site response spectra by the local site conditions ($\log_{10} f_s(T) = F_S$). We assumed the shape factor f_s at the seismic station can be obtained from the average H/V response spectral ratio (HVRSR), normalized by the average HVRSR at a reference rock site (Di Alessandro et al. 2012a). In a first step, we classified the stations into different soil classes (Table 2) because we found that amplification was observed as narrow bands in different period ranges of their average HVRSRs (see Fig. S2 in the Electronic Supplement).

We calculated the predominant period T^* of a station as the period at which the average HVRSR of its records has an unique peak value P^* (Zhao et al. 2006a; Fukushima et al. 2007; Di Alessandro et al. 2012a). If the average HVRSR was lower than 2 for the entire period range observed, the station was classified as reference rock site s_1. If the average HVRSR had multiple peaks or broad band amplification, the station was classified as

Table 2 Predominant period T^* site classification

SC	T^* (s)	No. of stations	No. of records
s_I	Not identifiable: HVRSR ≤ 2	35	340
s_{II}	$T^* \leq 0.2$	15	104
s_{III}	$0.2 < T^* \leq 0.4$	33	237
s_{IV}	$0.4 < T^* \leq 0.8$	28	241
s_V	$T^* > 0.8$	11	39
s_{VI}	Not identifiable: BB amplification or 2+ peaks	32	154
Total		154	1115

generic soil s_{VI}. Soil sites s_{II}, s_{III}, s_{IV}, and s_V were classified depending on T^* according to Table 2. We classified 154 seismic station sites using 1116 strong motion records of interface and intraslab earthquakes, a data subset of the complete Chilean earthquake database used in this study that satisfies our signal processing criteria (examples are shown in Fig. S2 of the Electronic Supplement). In contrast with the GMPE data subset selection, no magnitude-dependent limits to distance were applied this time. We succeeded in classifing the 79% of the total number of seismic stations using this approach (stations that are not classified as s_{VI}), which is equivalent to 86% of the total number of records. Similar percentages of successful classifications were obtained by Di Alessandro et al. (2012a).

For a given seismic station site, the f_s factor in Eq. (8) was defined as

$$f_s(sta)(T) = \frac{HVRSR_{(sta)}}{HVRSR_{(I)}} = \frac{S_{hs}/S_{vs}}{S_{hr}/S_{vr}}(T) \tag{9}$$

where $\text{HVRSR}_{(sta)}$ is the average HVRSR at the seismic station, $\text{HVRSR}_{(I)}$ is the average HVRSR of the reference rock sites s_I, S_{vs} is the vertical response spectra at a given soil site condition, and S_{vr} is the vertical response spectra at a rock site. Hence, Eq. (8) yields:

$$S_{hs}(T) = S_{hr}\frac{S_{hs}/S_{vs}}{S_{hr}/S_{vr}}(T) = S_{vr}\frac{S_{hs}}{S_{vs}}(T) \tag{10}$$

Assuming that the vertical component of ground motion at the soil site does not amplify relative to the vertical component in the rock site ($S_{vr} = S_{vs}$), the use of $f_s(sta) = \text{HVRSR}_{(sta)}/\text{HVRSR}_{(I)}$ is justified. It is worth noting that $\text{HVRSR}_{(I)}$ was approximately 1.4 in the studied period domain (see Fig. 2a).

Figure 2a, b show the average HVRSR and the standard deviation of all the seismic stations classified with the predominant period criteria from s_I to s_{VI}. The soil site classification as a function of T^* in Fig. 2a shows that the average spectra of each of the six site classes have relativity similar shape and amplitude, except for the reference rock site s_I and the generic soil s_{VI}. However, the standard deviations associated to Fig. 2a, b show that the maximum standard deviation is reached near P^* for every site class. This means that for similar T^* values the narrow amplification bands have different amplification levels (P^*). To account for this amplitude variability, we adopted an additional classification criterion based on the average HVRSR maximum amplitude P^* of a given station. If $2 < P^* \leq 3$, the soil was classified as A; if $3 < P^* \leq 4$, the soil was classified as B; and if $P^* > 4$, the soil was classified as C. For instance, if the site had a predominant period $T^* = 0.15$ s and its

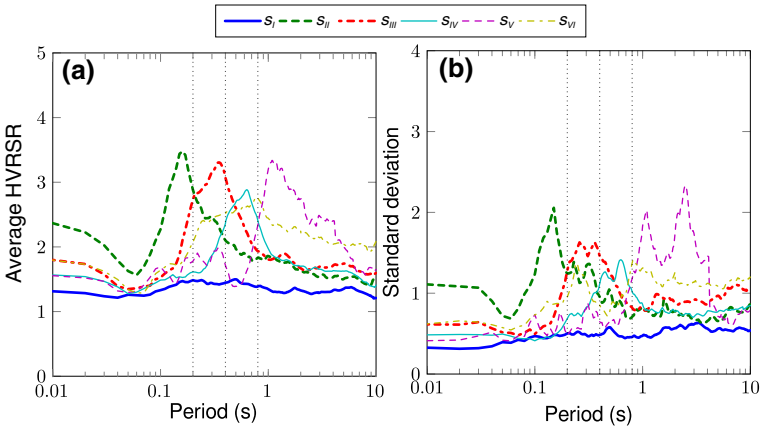

Fig. 2 **a** Average H/V response spectral ratios (HVRSRs) and their (**b**) standard deviations for site classes s_I, s_{II}, s_{III}, s_{IV}, s_V, and s_{VI}. The description of every class and the number of stations and records used in the computations are shown in Table 2

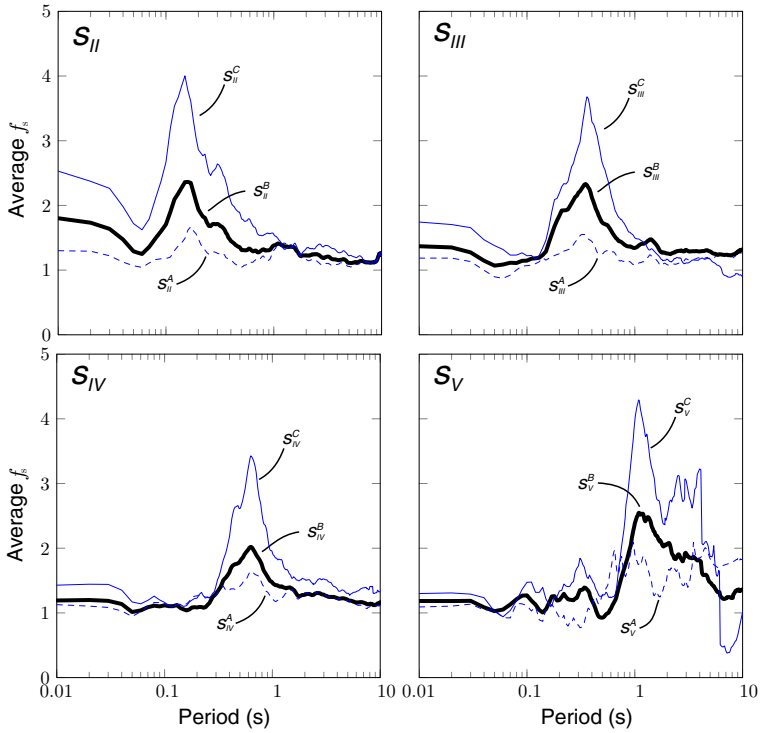

Fig. 3 Average site effect coefficients f_s computed for soil classes A, B and C in soil sites s_{II}, s_{III}, s_{IV}, and s_V

HVRSR maximum amplitude was $P^* = 3.5$, then the soil was classified as s_{II}^B. As there was no clear evidence of a relation between T^* and P^* we treated them as independent parameters.

Figure 3 shows the average f_s factors for the l amplitude classes A, B, and C at each k soil site class (k = II, III, IV, or V). For each soil site s_k, the thick solid line represents the average f_s factor for the amplitude class B (s_k^B), the dashed line the average f_s factor for the amplitude class A (s_k^A), and the thin solid line the average f_s factor for the amplitude class C (s_k^C).

For every soil site class s_k in Fig. 3, the average f_s factors of the soil site s_k^A and soil site s_k^C can be written in terms of the average f_s factor of the soil site s_k^B introducing new parameters n_A and n_C, respectively,

$$f_s(s_k^A) = \left[f_s(s_k^B)\right]^{n_A} \tag{11}$$

and

$$f_s(s_k^C) = \left[f_s(s_k^B)\right]^{n_C} \tag{12}$$

Using the peak values of the average f_s factors shown in Fig. 3, we computed the n_A and n_C that satisfied Eqs. 11 and 12 for each soil site s_k. These n values are a measure of the variation of P^*. Since T^* and P^* are independent parameters, the same values of n_A and n_C should be considered for every soil site class s_k. Then, the weighted averages of the n_A and n_C values for each soil class were computed using weights equal to the number of records in every soil site s_k. The calculated average values were $n_A = 0.666$ and $n_C = 1.730$ and the standard deviations were 0.13 and 0.26, respectively.

In addition, the average f_s factor of the soil site s_k^B is similar to the average f_s factor of the complete site class s_k, hence, the f_s factor in Eq. (8) can be evaluated as

$$f_s(T) = [f_s(s_k)]^n = \left(\frac{HVRSR_{(k)}}{HVRSR_{(I)}}\right)^n \tag{13}$$

where $\mathrm{HVRSR}_{(k)}$ is the average HVRSR of the soil site s_k or that of the generic soil site s_{VI}, and

$$n = \begin{cases} 0.666; & 2 < P^* \leq 3 \\ 1.730; & P^* > 4 \\ 1; & otherwise \end{cases} \tag{14}$$

Many seismic design codes, such as the NEHRP Provisions and the UBC, have used the V_{S30} to account for site effects (Dobry et al. 2000). Choi and Stewart (2005) represent the linear site effect coefficient (f_{lin}) as a function of V_{S30} as

$$f_{lin} = \left(\frac{V_{S30}}{V_{ref}}\right)^{s(T)} \tag{15}$$

where V_{ref} is a constant and $s(T)$ is a period dependent parameter. In the f_{lin} model in Eq. (15), the amplification level is described by the V_{S30} parameter and the shape of the amplification by the $s(T)$ parameter. As the n parameter in Eq. (13) describes the amplification level in our site effect model, we explored different empirical relationships between n and V_{S30}. Using a subset of 53 available V_{S30} measurements for sites of the

Chilean seismic stations (Arango et al. 2011; Boroschek et al. 2012, Fundación Chile de Investigación Geotécnica, FUCHIGE) and the n values obtained in this study, we ran different weighted least squares interpolations between both parameters. The regression with the lowest goodness-of-fit was obtained using the empirical relation

$$n = b \log_{10}\left(\frac{V_{S30}}{V_{ref}}\right) \tag{16}$$

where $b = -2.1396$ and $V_{ref} = 1530$ m/s (see Fig. S2 in the Electronic Supplement). If we impose that f_{lin} equals f_s, our model becomes a general case of the f_{lin} model in Eq. (15) where the shape of the amplification described by $s(T)$ is not constant and it depends on the predominant period of the soil T^*. Replacing Eq. (16) in $f_{lin} = f_s$, it can be shown that,

$$s_{T^*}(T) = b \log_{10}\left(\frac{HVRSR_{(k)}}{HVRSR_{(I)}}\right) \tag{17}$$

Finally, the site contribution term F_S in Eq. (2), which describes the soil site's response spectra relative to a reference rock site s_I, can be evaluated as a function of T^* and V_{S30}

$$F_S = F_S(V_{S30}, T^*) = \log_{10}(f_s) = s_{T^*}(T) \log_{10}\left(\frac{V_{S30}}{V_{ref}}\right) \tag{18}$$

Table 3 Site effect coefficients s_{T^*} for different soil sites

Period (s)	s_{II}	s_{III}	s_{IV}	s_V	s_{VI}
PGA	−0.584	−0.322	−0.109	−0.095	−0.212
0.01	−0.523	−0.262	−0.100	−0.092	−0.193
0.02	−0.459	−0.208	−0.092	−0.089	−0.177
0.03	−0.390	−0.160	−0.085	−0.088	−0.164
0.05	−0.306	−0.088	−0.075	−0.090	−0.146
0.07	−0.351	−0.056	−0.069	−0.096	−0.141
0.10	−0.524	−0.087	−0.070	−0.113	−0.156
0.15	−0.691	−0.336	−0.095	−0.166	−0.245
0.20	−0.671	−0.547	−0.127	−0.209	−0.359
0.25	−0.584	−0.674	−0.178	−0.235	−0.444
0.30	−0.506	−0.730	−0.258	−0.234	−0.491
0.40	−0.386	−0.718	−0.423	−0.164	−0.535
0.50	−0.300	−0.635	−0.537	−0.110	−0.557
0.75	−0.276	−0.395	−0.575	−0.358	−0.599
1.00	−0.275	−0.254	−0.462	−0.670	−0.584
1.50	−0.249	−0.238	−0.300	−0.801	−0.522
2.00	−0.218	−0.231	−0.220	−0.746	−0.479
3.00	−0.180	−0.219	−0.210	−0.628	−0.461
4.00	−0.171	−0.218	−0.212	−0.531	−0.448
5.00	−0.168	−0.218	−0.203	−0.438	−0.439
7.50	−0.168	−0.218	−0.153	−0.256	−0.435
10.00	−0.168	−0.218	−0.125	−0.231	−0.435

This results should be used to evaluate the F_S term in Eq. (18)

For the reference rock sites s_I, it should be assumed that there is no dynamic amplification and $s_{T^*}(T) = 0$. Soil sites with non-identifiable predominant period or broad band amplification should be considered as generic soil s_{VI}. For generic soil s_{VI} and identifiable predominant period soils, $s_{T^*}(T)$ values are shown in Table 3 and should be used following the predominant period site classification described in Table 2. If the T^* parameter cannot be determined because of the lack of seismic records at a given site, an approximation to it can be obtained from the H/V spectral ratio computed using microtremors time series recorded at the site and the Nakamura (1989) technique.

5 Regression methodology

The two-stages maximum likelihood regression method proposed by Joyner and Boore (1993) was used for different 5%-damped acceleration response spectra and PGA data. The site effect contribution to the response spectra was decoupled using the Eq. (8) and the empirical site effect coefficient described in Eq. (13).

5.1 First stage: path effects

At the first stage, the F_D coefficients of Eq. (5) were determined. The first regression for the first stage showed coefficients that represented non-physical behaviour (e.g. a positive geometrical spreading term and a positive anelastic term). We interpreted these results as a trade-off between coefficients due to the high dispersion of our strong motion data. To avoid this problem, we fixed the value of $c_4 = 0.1$ for the geometrical spreading magnitude-dependent effect (a similar value was adopted by Abrahamson et al. 2016). Also, $M_r = 5$ was fixed as a reference magnitude that gave the starting point to different magnitude-scaling effects. Second, we ran first-stage regressions using a temporary fixed value of $c_5 = -0.0015$ for anelastic attenuation effect. This c_5 temporary value was selected from the lowest standard deviation of three trial first-stage regression tests ran with $c_5 = -0.001$, $c_5 = -0.0015$, and $c_5 = -0.002$. The final first-stage regressions were ran using the geometrical spreading coefficients obtained previously (c_3 and Δc_3) to get the final anelastic coefficient values (c_5) and the intra-event standard deviations (σ_r).

The coefficients of the term R_o, which represent the near seismic source saturation effect with magnitude, were always fixed at $c_6 = 5$ and $c_7 = 0.35$. This choice generated a similar delay effect of attenuation with distance than that proposed by Atkinson and Boore (2003) and Abrahamson et al. (2016).

In the results of the first regression that we made, the first-stage residuals showed a trend with hypocentral depth for intraslab earthquakes, and it justified the addition of the depth term $c_8(H - h_o)$ in the seismic source term (F_F) of the functional form. No trends with hypocentral depth were found for interface earthquakes so this term was not added for them.

5.2 Second stage: seismic source

Using the results of the first-stage, second-stage weighted regressions were ran to determine the F_F free coefficients in Eq. (3). An uniform diagonal weight matrix whose elements are inversely proportional to the second-stage squared standard deviation for events with more than one record and zero for otherwise was used. Other definitions of the weight

matrix were also tested, such as the inverse of variance-covariance of second-stage residuals vector and a diagonal matrix with elements proportional to number of records for each event. We decided to use the weight matrix definition because it led to the lower second-stage (inter-event) standard deviation (σ_e).

At the first second-stage regression, we used the linear function $c_1 + c_2 M_w$ for F_F magnitude scaling, following the recommendations of Atkinson and Boore (2003) and Zhao et al. (2006b). Nevertheless, the quadratic term $c_9 M_w^2$ was added after the second-stage residual analysis because of the saturation effect shown with magnitude in Fig. 6. The need for a quadratic term was not clear for intraslab earthquakes, thus we decided to keep the linear function in this case.

6 Results

6.1 Coefficients and residuals

Table 4 shows the final results of the first-stage regressions smoothed with a linear fit using a number of points equal to 20% of the total coefficient vector length. The coefficients in Table 4 should be used to evaluate the path contribution term F_D in Eq. (5) to the response spectra. The first-stage residuals for different periods as a function of the source distance are shown in Fig. 4 for subsets of different magnitude. Figure 5 shows the same residuals

Table 4 Standard deviation and coefficient results of the first stage of the regression methodology

Period (s)	c_3	c_5	Δc_3	σ_r
PGA	−0.97558	−0.00174	−0.52745	0.232
0.01	−1.02993	−0.00175	−0.50466	0.231
0.02	−1.08567	−0.00176	−0.48043	0.233
0.03	−1.15951	−0.00176	−0.42490	0.235
0.05	−1.28640	−0.00178	−0.31239	0.241
0.07	−1.34644	−0.00181	−0.17995	0.251
0.10	−1.32353	−0.00182	−0.13208	0.255
0.15	−1.17687	−0.00183	−0.26451	0.255
0.20	−1.04508	−0.00182	−0.39105	0.268
0.25	−0.94363	−0.00178	−0.34348	0.264
0.30	−0.84814	−0.00173	−0.36695	0.260
0.40	−0.69278	−0.00166	−0.46301	0.263
0.50	−0.57899	−0.00161	−0.54098	0.261
0.75	−0.56887	−0.00158	−0.46266	0.252
1.00	−0.53282	−0.00154	−0.42314	0.247
1.50	−0.46263	−0.00145	−0.58519	0.246
2.00	−0.40594	−0.00139	−0.65999	0.245
3.00	−0.33957	−0.00137	−0.79004	0.231
4.00	−0.26479	−0.00137	−0.86545	0.228
5.00	−0.22333	−0.00137	−0.88735	0.232
7.50	−0.30346	−0.00131	−0.91259	0.231
10.00	−0.33771	−0.00117	−0.96363	0.204

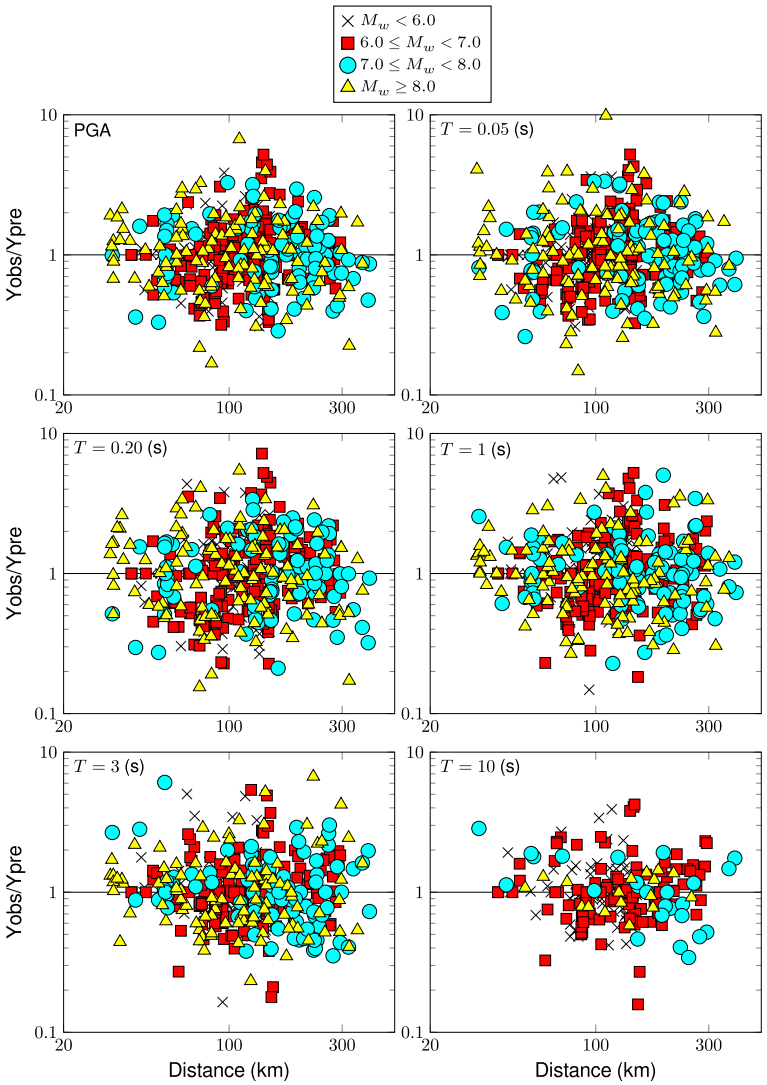

Fig. 4 First-stage (within-event) residuals for different periods versus distance. The residual is computed as the ratio between the observed value over the predicted value, and the results are grouped into different magnitude subsets

for subsets of different site class. The residuals were obtained as the ratio between observed data and the first-stage prediction results. No clear trends could be identified in Figs. 4 and 5 at any regression period.

Table 5 shows the final results from the second-stage regressions. The coefficients were smoothed using the same function used at the first-stage results and they should be used to evaluate the source contribution term F_F in Eq. (3). In addition, the global standard deviation (σ_t in Table 5) was computed for every regression period as $\sigma_t = \sqrt{\sigma_e^2 + \sigma_r^2}$.

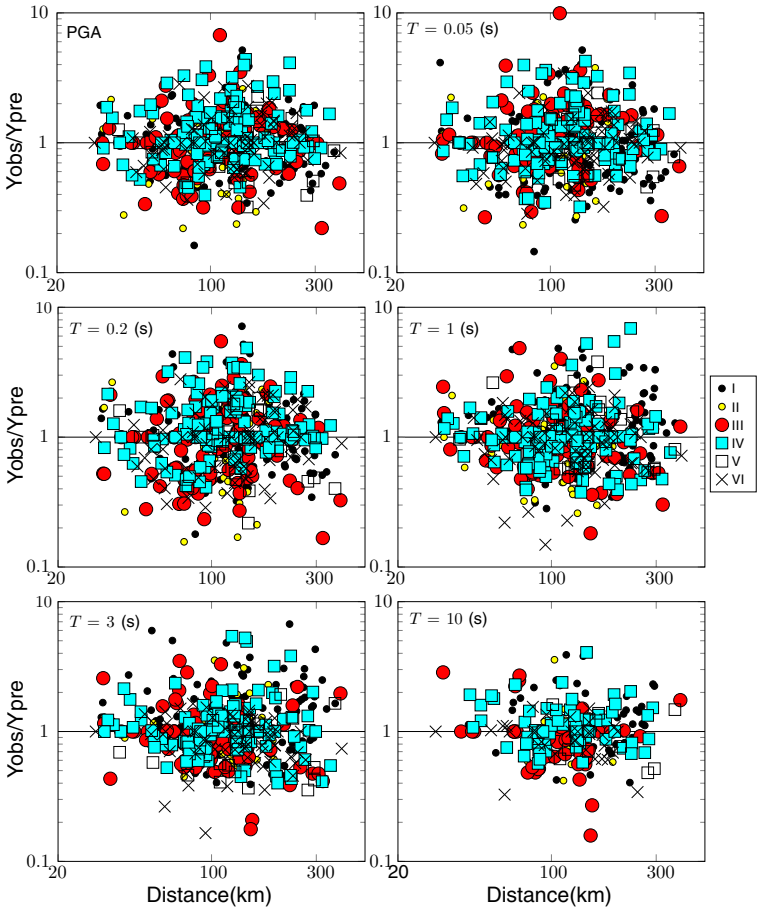

Fig. 5 First-stage (within-event) residuals for different periods versus distance. The residual is computed as the ratio between the observed value over the predicted value, and the results are grouped into different site class subsets

Figure 6 shows the event data ($\hat{F}_F$) used in the second stage for intraslab and interface earthquakes. The F_F term predictions are also shown in Fig. 6 as a solid line for interface earthquakes and dotted line for intraslab earthquakes. The event data of Fig. 6 is normalized to the same hypocentral depth and to the reference rock site s_I, and it shows a wider dispersion for events with smaller magnitudes. The F_F term predictions clearly fit the between-evet data for both earthquake types in Fig. 6.

6.2 Reference rock site data

Figure 7 shows ground-motion prediction results for different magnitude interface and intraslab earthquakes at reference rock site s_I. It compares ground motion predictions for PGA, $T = 1$ s, and $T = 3$ s with ground motion data normalized to a reference rock site s_I. A hypocentral depth of $H = 105$ km is used for intraslab earthquakes. The predictions are evaluated at distances from 30 to 400 km for interface earthquakes and from 60 to 400 km

Table 5 Standard deviation and coefficient results of the second stage of the regression methodology

Period (s)	c_1	c_2	c_9	c_8	Δc_1	Δc_2	σ_e	σ_t
PGA	−2.8548	0.7741	−0.03958	0.00586	2.5699	−0.4761	0.172	0.289
0.01	−2.8424	0.8052	−0.04135	0.00584	2.7370	−0.5191	0.173	0.288
0.02	−2.8337	0.8383	−0.04325	0.00583	2.9087	−0.5640	0.176	0.292
0.03	−2.8235	0.8838	−0.04595	0.00586	3.0735	−0.6227	0.178	0.295
0.05	−2.7358	0.9539	−0.05033	0.00621	3.2147	−0.7079	0.190	0.307
0.07	−2.6004	0.9808	−0.05225	0.00603	3.0851	−0.7425	0.213	0.329
0.10	−2.4891	0.9544	−0.05060	0.00571	2.8091	−0.7055	0.195	0.321
0.15	−2.6505	0.9232	−0.04879	0.00560	2.6260	−0.6270	0.160	0.302
0.20	−3.0096	0.9426	−0.05034	0.00573	2.6063	−0.5976	0.157	0.310
0.25	−3.3321	0.9578	−0.05143	0.00507	2.3654	−0.5820	0.142	0.299
0.30	−3.5422	0.9441	−0.05052	0.00428	2.2017	−0.5412	0.141	0.296
0.40	−3.3985	0.7773	−0.03885	0.00308	1.6367	−0.3448	0.157	0.306
0.50	−2.8041	0.5069	−0.01973	0.00257	0.7621	−0.0617	0.152	0.302
0.75	−4.4588	0.8691	−0.04179	0.00135	2.1003	−0.4349	0.146	0.291
1.00	−5.3391	1.0167	−0.04999	0.00045	2.5610	−0.5678	0.153	0.290
1.50	−6.1204	1.1005	−0.05426	0.00068	2.8923	−0.5898	0.152	0.289
2.00	−7.0334	1.2501	−0.06356	0.00051	3.3941	−0.7009	0.157	0.291
3.00	−8.2507	1.4652	−0.07797	0.00066	4.0033	−0.8465	0.155	0.279
4.00	−8.7433	1.4827	−0.07863	0.00063	3.9337	−0.8134	0.160	0.279
5.00	−8.9927	1.4630	−0.07638	0.00067	3.7576	−0.7642	0.167	0.286
7.50	−9.8245	1.6383	−0.08620	0.00108	4.3948	−0.9313	0.164	0.283
10.00	−9.8671	1.5877	−0.08168	0.00014	4.3875	−0.8892	0.176	0.270

Global standard deviation is computed as $\sigma_t = \sqrt{\sigma_e^2 + \sigma_r^2}$

for intraslab earthquakes. The predictions in Fig. 7 show good agreement with the observations, except at some subfigures that exhibit explicit lack of data. For instance, the predictions of ground motion for intraslab earthquakes at long period are greater than the observed data (Fig. 7b; $T = 3$ s).

6.3 Site effects

The evaluation of ground motion predictions for different soil conditions at PGA, $T = 0.05$ s, $T = 1$ s, and $T = 3$ s are shown in Fig. 8. Only three site conditions are shown to avoid redundancy (s_I, s_{II}, and s_V). For PGA predictions, reference rock sites s_I are similar to soil sites s_V (very long T^*), and soil sites s_{II} (very short T^*) have the highest ground motion. On the other hand, for $T = 3$ s predictions, soil sites s_V have the highest accelerations, with similar lower accelerations for reference rock sites s_I and soil sites s_{II}. Figure 8 shows that the highest predicted values are obtained at the soil site that has the closest predominant period (T^*) to the ground motion period (T), while the lowest are obtained always at the reference rock site s_I. Figure 9 shows the predicted ground-motion response spectra (Sa) for interface and intraslab earthquakes at different site conditions: reference rock site s_I, soil site s_{II} and soil site s_V. A two-peak response spectra is predicted for soil site s_V in

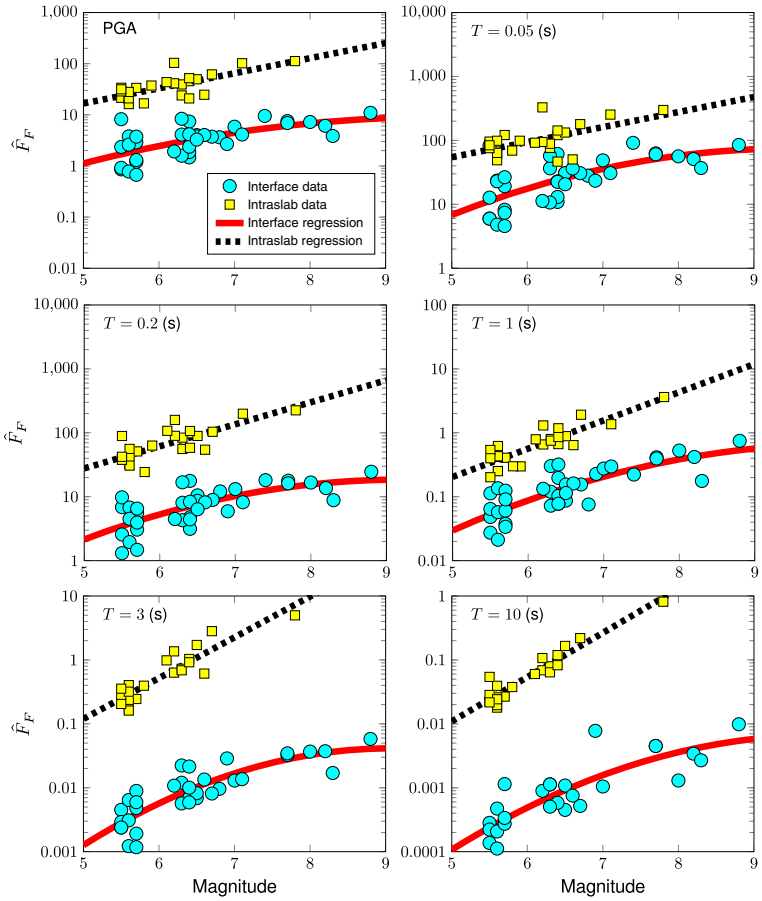

Fig. 6 Fit of the second-stage (between-event) results of the F_F term to the $\hat{F}_F$ data for different periods. The intraslab earthquake data is adjusted by a linear effect, and the intraslab earthquake data by a quadratic effect. The data is normalized to a reference rock site s_I

Fig. 9, which is a soil with a long predominant period. In the other hand, the predicted response spectra in Fig. 9 has only one peak at soil sites s_{II} (short predominant period) and at reference rock sites s_I. A value of $V_{S30} = 400$ m/s is used for soil sites at all predictions in Figs. 8 and 9.

6.4 Types of earthquakes

Two general behaviours can be identified from Figs. 7 and 8: a decrease in attenuation slopes with period, and a steeper attenuation slope for intraslab earthquakes compared to interface earthquakes. Figure 8 shows that the ground motion of intraslab earthquakes is specially high at close distances to the seismic source and then it decreases fast with distance, whereas the ground motion of interface earthquakes maintains a relative important intensity in a more extensive area.

The response spectra of ground motion predictions for intraslab and interface earthquakes are shown in Fig. 10. Different magnitudes and distances are evaluated for a

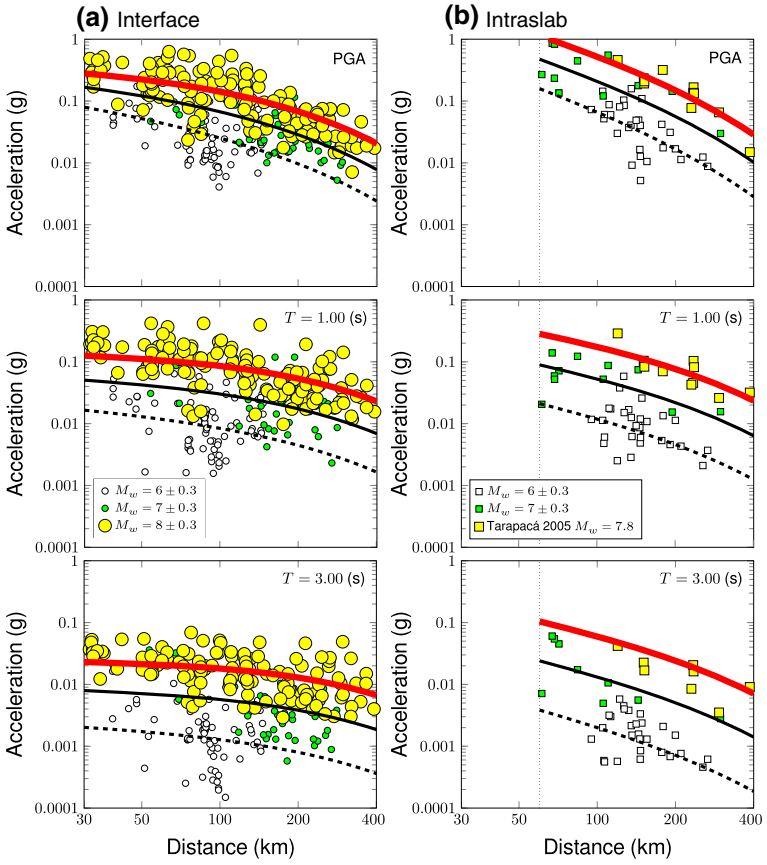

Fig. 7 Ground motion predictions for different period, magnitudes, and type of earthquake, considering a reference rock site s_I. The observed strong motion data has been included before a normalization to a reference rock site. **a** Interface earthquakes with *solid thick line* $M_w = 8$, *solid thin line* $M_w = 7$, and *dashed line* $M_w = 6$. **b** Intraslab earthquakes with *solid thick line* $M_w = 7.8$, *solid thin line* $M_w = 7$, and *dashed line* $M_w = 6$

reference rock site s_I. A smooth shape and consistent scaling with magnitude is observed for all response spectra from 0.01 to 10 s, and their peak values located around 0.1 to 0.2 s. Figure 10 shows that for close distances and depending on the depth of the seismic source, an intraslab earthquake generates higher ground motion than an interface earthquake of the same magnitude.

6.5 Comparison of the proposed GMPE with previous studies

Figure 11 compares the predictions of our GMPE with those of Atkinson and Boore (2003) (AB03), Zhao et al. (2006b) (Zea06) and Abrahamson et al. (2016) (Aea16). These studies were selected by the Global Earthquake Model (GEM) project (Stewart et al. 2015) as recommended for seismic hazard estimations in subduction zones. Arango et al. (2012) recommend their use for seismic hazard analysis in the Chile-Peru subduction zone. In addition to those three studies, the study of Contreras and Boroschek (2012)(CB12) for

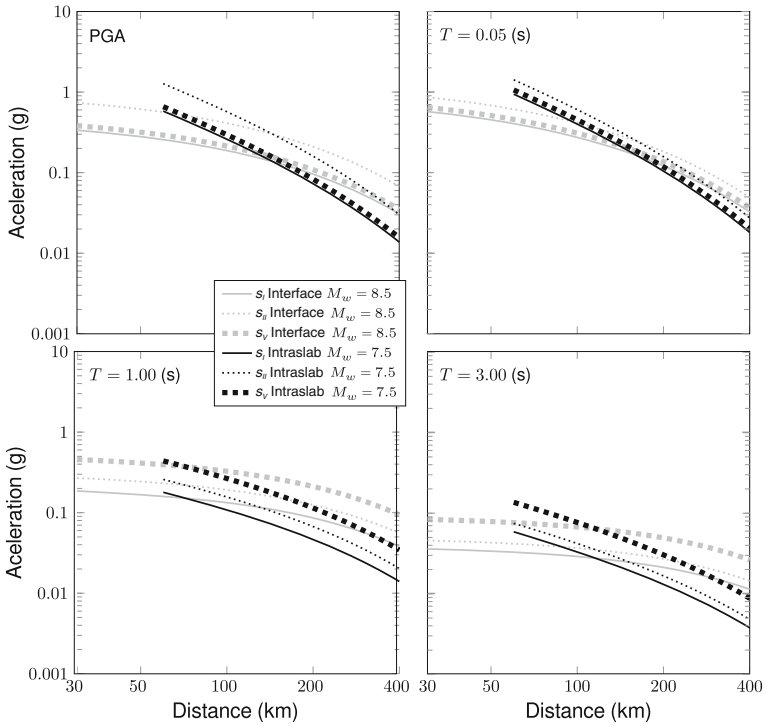

Fig. 8 Ground motion predictions for different periods and type of earthquake using different site conditions. A $V_{S30} = 400$ m/s is used in all cases. The interface earthquake predictions are for $M_w = 8.5$ and the intraslab earthquake predictions for $M_w = 7.5$

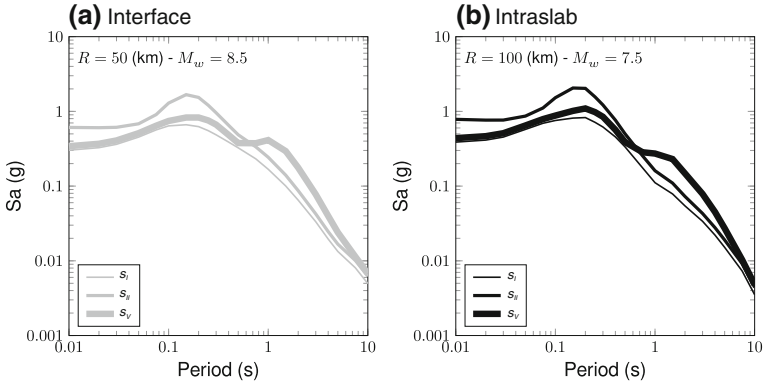

Fig. 9 Response spectra predicted for **a** $M_w = 8.5$ interface ($R = 50$ km) and **b** $M_w = 7.5$ intraslab ($R = 100$ km) earthquakes using different site conditions. A $V_{S30} = 400$ m/s is used in both soil site cases

Chilean interface earthquakes is included in Fig. 11. Rock site conditions or the closest definition to it, depending on the study, are used in all cases. The interface earthquake scenario in Fig. 11a is similar to the $M_w = 8.8$ Maule 2010 earthquake. In this case, the predictions of the proposed GMPE are similar to those of Atkinson and Boore (2003) and

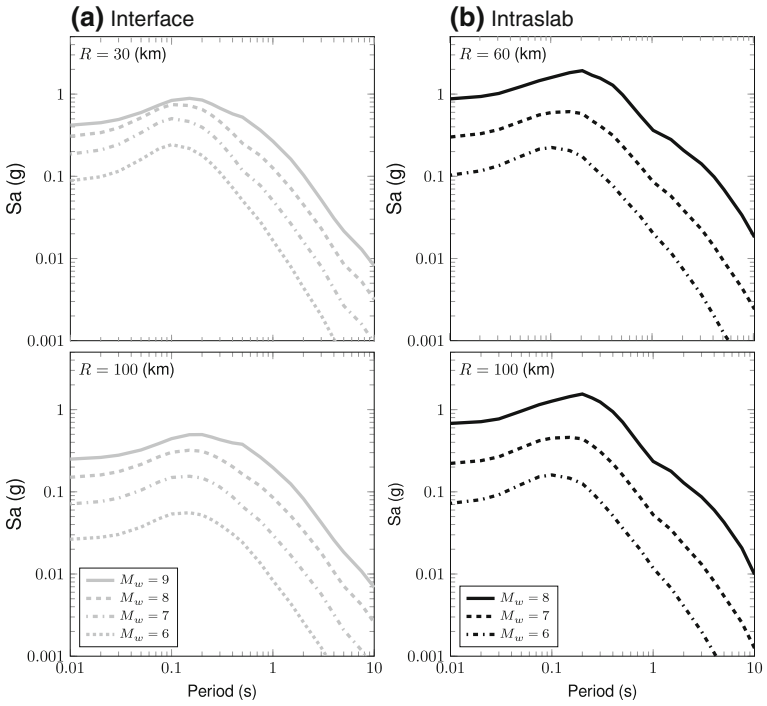

Fig. 10 Response spectra predicted for different magnitudes, distances, and type of earthquake for a reference rock site s_I. **a** Interface and **b** intraslab earthquakes

the Contreras and Boroschek et al. (2012). Nevertheless, there is a difference in PGA that becomes higher for short distances. The Zhao et al. (2006b) and Abrahamson et al. (2016) predictions show steeper attenuation slopes in Fig. 11a.

An intraslab earthquake GMPEs comparison is shown in Fig. 11b. A slab event with $M_w = 7.8$ and $H = 105.5$ km is used, similar to the 2005 Tarapacá earthquake. Atkinson and Boore (2003) have the most similar database to that used by us. As well as Abrahamson et al. (2016), they show similar preditions to those of our study for PGA in Fig. 11b. For longer periods, every GMPE in Fig. 11b shows similar predictions, with the Zhao et al. (2006b) GMPE being a lower bound in all cases. Our intraslab GMPE show a slightly flatter attenuation slope relative to other studies for long and mid-range periods.

Figure 12 shows the first-stage (within-event), second-stage (between-event), and total standard deviations obtained at every regression. The values obtained for the three measures of standard deviation are similar to those recommended by Abrahamson et al. (2016) to be used in seismic hazard analysis (dashed line in Fig. 12). The total standard deviation of the GMPE developed by Contreras and Boroschek (2012) for Chilean interface earthquakes is also shown in Fig. 12, and it has a similar value to the within-event standard deviation obtained in this study.

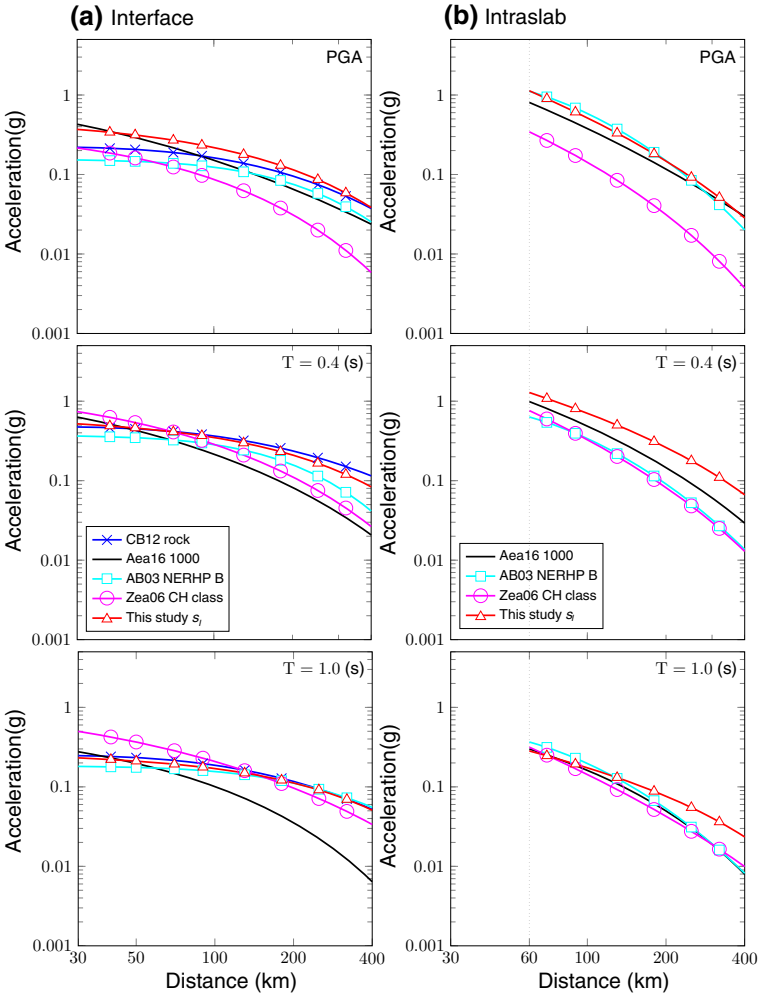

Fig. 11 Comparison of the proposed GMPE with previous studies for two cases using rock site conditions. **a** $M_w = 8.8$ interface earthquake, similar to the Maule 2010 earthquake. **b** $M_w = 7.8$ intraslab earhquake with hypocentral depth $H = 105.5$ (km), similar to the Tarapacá 2005 earthquake

7 Discussion

The final within-event and between-event residuals of Figs. 4, 5, and 6 do not show clear trends with any parameter as a consequence of the methodology applied in the selection of the functional form. New effects were added to the terms of the functional form when a trend was identified in the residuals and we continuously kept doing it until the residual plots showed no clear trend. Despite this method ensured a good fit to the present data, we anticipate that some of our decissions on the functional form selection should be reviewed when additional data of future earthquakes would be available. For example, long period intraslab $\hat{F}_F$ data in Fig. 6 may have also a quadratic effect of saturation with magnitude as

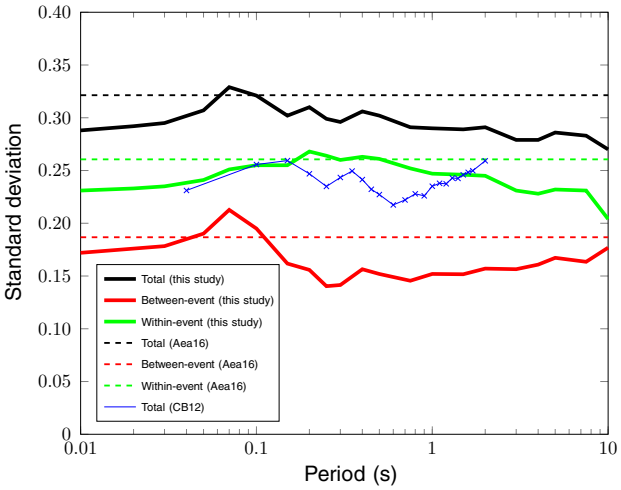

Fig. 12 Standard deviations (total, between-event, and within-event) obtained for all regressions. The standard deviations obtained in other studies are given as reference values

interface earthquakes have, but lack of data does not allowed us to draw solid conclusions on this matter.

Arango et al. (2012) found that Atkinson and Boore (2003), Zhao et al. (2006b), and Abrahamson et al. (2016) were the best fitting attenuation models for interface earthquake data of the Peru-Chile region, and that Zhao et al. (2006b) and Abrahamson et al. (2016) can be used in logic-tree branches for seismic hazard assessment of intraslab earthquakes in the same region. To select our functional form we used as reference the same GMPEs recommended by Arango et al. (2012).

In general, variations of T^* influence the shape of the site effects on the response spectra. As the site effect is represented as a modification over the reference rock site s_1 ground-motion response spectra, it is possible to predict a two-peak ground-motion response spectra for soil sites with long predominant period, as Fig. 9 shows. As Ruiz and Saragoni (2008) pointed out, in this situations one of the peaks represent the highest energy content of the earthquake while the other one the dynamic response of the soil.

On the other hand, variations of V_{S30} influence site effects in their amplitude. Higher V_{S30} values imply lower predicted accelerations for any predominant period. Values of V_{S30} lower than 400 m/s may cause non-linear effects that are not reproduced by our site effect model. For these low V_{S30} values, the predictions would overestimate the ground motion values. In consequence, future considerations of non-linear site effects in the site effect model presented in this work should reduce the ground motion amplitude for sites with low V_{S30} values.

The stepper attenuation slope of intraslab earthquakes relative to the attenuation slope of interface earthquakes is reproduced by the term $\Delta c_3 F_{eve}$ in Eq. (7) and it is consistent with previous results by Youngs et al. (1997) and Atkinson and Boore (2003). The negative value of $\Delta c_3 F_{eve}$ for every period implies a larger geometrical spreading value for intraslab earthquakes. As the anelastic attenuation value is the same for interface and intraslab earthquakes, the difference between the attenuation slope of both types of earthquake in Fig. 7 is controlled by the difference in the geometrical spreading values. The theoretical value of the geometrical spreading is $1/r$ for body waves and $1/\sqrt{(}r)$ for

surface waves (Aki and Richards 2002). As interface earthquakes have shallow-depth sources, we interpret that surface waves could have a stronger influence on the ground motion of them and also on their average attenuation slope relative to those of intraslab earthquakes.

The similar ground motion predictions for interface earthquakes of this study relative to that of Contreras and Boroschek (2012) and Atkinson and Boore (2003) shown in Fig. 11 are consistent with the fact that all of them included Chilean data in their databases. The larger PGA values predicted by our GMPE relative to that of Contreras and Boroschek (2012) may come from the use of recent contributions of Boore and Goulet (2014) to signal processing, such as limited high frequency filtering, which has effects in the response spectra at high frequencies. On the other hand, Zhao et al. (2006b) use almost exclusively Japanese earthquake records and Abrahamson et al. (2016) a Japanese earthquake biased database. Therefore, it is possible to interpret the difference in the attenuation slopes of interface earthquakes predicted by this study with those predicted by Zhao et al. (2006b) and Abrahamson et al. (2016) in Fig. 11 as a regional difference between Chilean and Japanese subduction zones. This observation confirms a flatter attenuation slope of the interface South American earthquakes relative to other regions (Stewart et al. 2015). The geometry of subduction zones and the location of the seismicity vary from one region to other producing different paths. This difference in the path that seismic waves follow from the source to the stations could be physically related to the difference in attenuation slopes between regions. On the other hand, general properties of the propagation media (as their quality factor) could also vary with the region. Assuming this condition, the anelastic attenuation should not be constant for every region leading to variations in the attenuation slope between regions.

The standard deviation of a GMPE model accounts for the level of uncertainty of a model when it is used to reproduce the data used in their derivation. It depends on the complexity of the functional form to account for different kind of effects but also on the different phenomena present on the ground motion data or its diversity. Given a functional form, regressions made over highly diverse data should show higher uncertainty (standard deviation) than those made on less-diverse data. In addition, given a database, regressions made using a complex but well-selected functional form should show less uncertainty than those regressions made using simpler functional forms. By well-selected functional form we mean those functional forms that includes only effects identified in the database. For example, despite the functional form used in this study was similar to that of Abrahamson et al. (2016) with exception to the site effect model, this study obtained lower standard deviations than Abrahamson et al. (2016) in a broad band of periods. This uncertainty difference can be explained by the low diversity of our Chilean database relative to the worldwide database used by Abrahamson et al. (2016). As an additional example,Contreras and Boroschek (2012) used a simpler functional form than ours and they got a lower standard deviation. In this case, the database used in our study included records from recent Chilean earthquakes that added diversity to the Chilean database used in the Contreras and Boroschek (2012) GMPE.

The selection of the distance metrics is spected to has a strong influence on the within-event standard deviation. Despite that for large magnitude interface earthquakes the closest distance to the rupture area introduces less artificial uncertainty than using the distance to the hypocenter, it is not a perfect metric of distance because seismic waves are not emitted with the same intensity from every point of the rupture area. Instead of that, the emission of waves of greater intensity concentrates in zones inside the rupture area called asperities. The use of the closest distance to the rupture area was preferred over the distance to the

asperity because asperities are not easy to locate resulting in additional complications for the user of the GMPE.

8 Conclusion

Since 2010, three thrust interface earthquakes of $M_w \geq 8.2$ have affected the Chilean subduction zone, the 2014 $M_w = 8.2$ Iquique earthquake, the 2015 $M_w = 8.3$ Illapel earthquake, and the 2010 $M_w = 8.8$ Maule megathrust earthquake. The records gathered from these earthquakes have helped to close the gap for megathrust earthquakes in the Chilean ground motion database. Using a database with only Chilean earthquakes, which include records from these last three events, a GMPE for peak ground acceleration (PGA), and response spectral accelerations (Sa) with 5% damping ratio for periods between 0.01 and 10 s is developed. This study satisfies some of the Next Generation Attenuation (NGA) project requirements (Power et al. 2008), such as ground motion prediction for periods between 0.01 and 10 s and earthquake magnitudes starting at $M_w = 5.5$. Some of the selection criteria of the Global Earthquake Model (GEM) (Di Alessandro et al. 2012b) is incorporated as well, such as a functional form that considers saturation with magnitude, magnitude-dependent distance scaling, and anelastic attenuation. Also, this study satisfies the exclusion criteria proposed by Bommer et al. (2010) with exception of the dataset size, which would be too strict to be applied for subduction zones. The proposed GMPE can predict the ground motion of large Chilean subduction earthquakes ($M_w > 8$) with no need of extrapolation from small-magnitude earthquake data.

Different attenuation slopes were identified for interface and intraslab Chilean earthquakes. For close distances, the intraslab earthquake ground motions can be larger than those of interface ones. Nevertheless, the attenuation is higher for intraslab earthquakes, which reduces the potential affected area. These results are consistent with those reported by Youngs et al. (1997)and Atkinson and Boore (2003) for world wide subduction zones.

As we only used Chilean earthquake data, we looked for possible regional attenuation differences between Chile and Japan through the comparison of our model with GMPEs derived from large magnitude well-recorded Japanese earthquakes ($M_w > 8.0$) (Zhao et al. 2006b). Chilean interface earthquakes showed a flatter attenuation slope compared to Japanese interface earthquakes, which implies that regional variations of ground motion should be taken in consideration for seismic hazard analysis and future GMPE derivation.

The proposed equations can be used for interface earthquakes at rupture distances from 30 to 400 km and magnitudes $M_w \leq 9$, and for intraslab earthquakes with hypocentral distances from 60 to 400 km, hypocentral depths $H \leq 150$ km, and magnitudes $M_w \leq 8$. The user of the GMPE should evaluate Eq. (2), which terms are defined in Sects. 3 and 4. Tables 4 and 5 should be used to evaluate the path term and the source term. To evaluate the site effect term, the user needs to know the V_{S30} and the T^* parameters of the site. From the T^* value, the site should be classified using the classification of Table 2. Finally, the site effect term should be evaluated using the coefficients of Table 3 given for the appropriate site class. The site effect term derived in this study is not recommended for sites with $V_{S30} < 400$ m/s.

Acknowledgements This study was partially financially supported by Chile's National Commission on Scientific and Technological Research (CONICYT) for the Fondecyt Initiation into Research 2014 projects, National Research Funding Competition under Grant Nos. 11140429 and 11130230, and by CONICYT-

PCHA/MagísterNacional/2014 - 22140466. We are grateful to RENADIC and CSN, both from the University of Chile, for transfering the raw data of their networks to us.

References

Abrahamson N, Gregor N, Addo K (2016) BC hydro ground motion prediction equations for subduction earthquakes. Earthq Spectra 32(1):23–44. doi:10.1193/051712EQS188MR

Aki K, Richards PG (2002) Quantitative seismology, 2nd edn. University Science Books, Sausalito

Akkar S, Bommer JJ (2006) Influence of long-period filter cut-off on elastic spectral displacements. Earthq Eng Struct 35(9):1145–1165. doi:10.1002/eqe.577

Atkinson GM, Boore DM (2003) Empirical ground-motion relations for subduction-zone earthquakes and their application to Cascadia and other regions. Bull Seismol Soc Am 93(4):1703–1729. doi:10.1785/0120020156

Arango MC, Strasser FO, Bommer JJ, Boroschek R, Comte D, Tavera H (2011) A strong-motion database from the Peru–Chile subduction zone. J Seismol 15(1):19–41. doi:10.1007/s10950-010-9203-x

Arango MC, Strasser FO, Bommer JJ, Cepeda JM, Boroschek R, Hernandez DA, Tavera H (2012) An evaluation of the applicability of current ground-motion models to the south and central American subduction zones. Bull Seismol Soc Am 102(1):143–168. doi:10.1785/0120110078

Arroyo D, García D, Ordaz M, Mora MA, Singh SK (2010) Strong ground-motion relations for Mexican interplate earthquakes. J Seismol 14(4):769–785. doi:10.1007/s10950-010-9200-0

Béjar-Pizarro M, Carrizo D, Socquet A, Armijo R, Barrientos S, Bondoux F, Bonvalot S, Campos J, Comte D, de Chabalier JB, Charade O, Delorme A, Gabalda G, Galetzka J, Genrich J, Nercessian A, Olcay M, Ortega F, Ortega I, Remy D, Ruegg JC, Simons M, Valderas C, Vigny C (2010) Asperities and barriers on the seismogenic zone in North Chile: state-of-the-art after the 2007 Mw 7.7 Tocopilla earthquake inferred by GPS and InSAR data. Geophys J Int 183(1):390–406

Bommer JJ, Douglas J, Scherbaum F, Cotton F, Bungum H, Fäh D (2010) On the selection of ground-motion prediction equations for seismic hazard analysis. Seismol Res Lett 81(5):783–793. doi:10.1785/gssrl.81.5.783

Boore DM (2003) Simulation of ground motion using the stochastic method. Pure Appl Geophys 160(3–4):635–676. doi:10.1007/PL00012553

Boore DM (2005) On pads and filters: processing strong-motion data. Bull Seismol Soc Am 95(2):745–750. doi:10.1785/0120040160

Boore DM, Bommer JJ (2005) Processing of strong-motion accelerograms: needs, options and consequences. Soil Dyn Earthq Eng 25(2):93–115. doi:10.1016/j.soildyn.2004.10.007

Boore DM, Goulet CA (2014) The effect of sampling rate and anti-aliasing filters on high-frequency response spectra. Bull Earthq Eng 12(1):203–216. doi:10.1007/s10518-013-9574-9

Boroschek RL, Contreras V, Kwak DY, Stewart JP (2012) Strong ground motion attributes of the 2010 M_w Maule, Chile, earthquake. Earthq Spectra 28(S1):19–38. doi:10.1193/1.4000045

Choi Y, Stewart JP (2005) Nonlinear site amplification as function of 30 m shear wave velocity. Earthq Spectra 21(1):1–30. doi:10.1193/1.1856535

Christensen DH, Ruff LJ (1986) Rupture process of the March 3, 1985 Chilean earthquake. Geophys Res Lett 13(8):721–724

Contreras V, Boroschek R (2012) Strong ground motion attenuation relations for Chilean subduction zone interface earthquakes. In: Proccedings in 15th world conference on earthquake engineering, Lisboa, Portugal

Cotton F, Scherbaum F, Bommer JJ, Bungum H (2006) Criteria for selecting and adjusting ground-motion models for specific target regions: application to central Europe and rock sites. J Seismol 10(2):137–156. doi:10.1007/s10950-005-9006-7

Di Alessandro C, Bonilla LF, Boore DM, Rovelli A, Scotti O (2012a) Predominant-period site classification for response spectra prediction equations in Italy. Bull Seismol Soc Am 102(2):680–695. doi:10.1785/0120110084

Di Alessandro C, Bozorgnia Y, Abrahamson NA, Akkar S, Erdik M (2012b) GEM-PEER global ground motion prediction equations project: an overview. In: Proccedings in the 15th world conference on earthquake engineering, pp 24–28

Dobry R, Borcherdt RD, Crouse CB, Idriss IM, Joyner WB, Martin GR, Power MS, Rinne EE, Seed RB (2000) New site coefficients and site classification system used in recent building seismic code provisions. Earthquake Spectra 16(1):41–67

Douglas J, Boore DM (2011) High-frequency filtering of strong-motion records. Bull Earthq Eng 9(2):395–409. doi:10.1007/s10518-010-9208-4

Edwards B, Fäh D (2013) Measurements of stress parameter and site attenuation from recordings of moderate to large earthquakes in Europe and the Middle East. Geophys J Int 194(2):1190–1202. doi:10.1093/gji/ggt158

Ekström G, Nettles M, Dziewonski AM (2012) The global CMT project 2004–2010: centroid-moment tensors for 13,017 earthquakes. Phys Earth Planet Inter 200–201:1–9. doi:10.1016/j.pepi.2012.04.002

Engdahl ER, Villaseñor A (2002) 41 Global seismicity: 1900–1999. Int Geophysics 81:665-XVI

Fundación Chile de Investigación Geotécnica (FUCHIGE). www.fuchige.cl. Accessed Dec 2015

Fukushima Y, Bonilla LF, Scotti O, Douglas J (2007) Site classification using horizontal-to-vertical response spectral ratios and its impact when deriving empirical ground-motion prediction equations. J Earthq Eng 11(5):712–724

García D, Singh SK, Herráiz M, Ordaz M, Pacheco JF (2005) Inslab earthquakes of central Mexico: peak ground-motion parameters and response spectra. Bull Seismol Soc Am 95(6):2272–2282. doi:10.1785/0120050072

Gregor NJ, Silva WJ, Wong IG, Youngs RR (2002) Ground-motion attenuation relationships for Cascadia subduction zone megathrust earthquakes based on a stochastic finite-fault model. Bull Seismol Soc Am 92(5):1923–1932. doi:10.1785/0120000260

Hayes GP, Wald DJ, Johnson RL (2012) Slab1.0: A three-dimensional model of global subduction zone geometries. J Geophys Res 117(B1): doi:10.1029/2011JB008524

International Seismological Centre (ISC). www.isc.ac.uk/iscbulletin. Accessed Oct 2015

Joyner WB, Boore DM (1993) Methods for regression analysis of strong-motion data. Bull Seismol Soc Am 103(2A):1069–1084

Lin PS, Lee CT (2008) Ground-motion attenuation relationships for subduction-zone earthquakes in northeastern Taiwan. Bull Seismol Soc Am 98(1):220–240. doi:10.1785/0120060002

McVerry GH, Zhao JX, Abrahamson NA, Somerville PG (2006) New Zealand acceleration response spectrum attenuation relations for crustal and subduction zone earthquakes. Bull N Z Soc Earthq Eng 39(1):1–58

Mendoza M, Hartzell S, Monfret T (1994) Wide-band analysis of the 3 March 1985 Central Chile earthquake: overall source process and rupture history. B Seismol Soc Am 84(2):269–283

Moreno M, Melnick D, Rosenau M, Baez J, Klotz J, Oncken O, Tassara A, Chen J, Bataille K, Bevis M, Socquet A, Bolte J, Vigny C, Brooks B, Ryder I, Grund V, Smalley B, Carrizo D, Bartsch M, Hase H (2012) Toward understanding tectonic control on the Mw 8.8 2010 Maule Chile earthquake. Earth Planet Sci Lett 321–322:152–165

Nakamura, Y (1989) A method for dynamic characteristics estimation of subsurface using microtremor on the ground surface. Railway Technical Research Institute, Quarterly Reports, vol 30, no 1

National Accelerometer Network of the Department of Civil Engineering (RENADIC), University of Chile. terremotos.ing.uchile.cl. Accessed Oct 2015

National Seismological Center (CSN), University of Chile. www.sismologia.cl. Accessed Oct 2015

Otarola C, Ruiz S (2016) Stochastic generation of accelerograms for subduction earthquakes. Bull Seismol Soc Am 106(6): doi:10.1785/0120150262

Peyrat S, Madariaga R, Buforn E, Campos J, Asch G, Vilotte JP (2010) Kinematic rupture process of the 2007 Tocopilla earthquake and its main aftershocks from teleseismic and strong-motion data. Geophys J Int 182(3):1411–1430. doi:10.1111/j.1365-246X.2010.04685.x

Power M, Chiou B, Abrahamson N, Bozorgnia Y, Shantz T, Roblee C (2008) An overview of the NGA project. Earthq Spect 24(1):3–21. doi:10.1193/1.2894833

Ruiz S, Saragoni RG (2008) Two peaks response spectra (2PRS) for subduction earthquakes considering soil and source effects. In: Proccedings in the 14th world conference on earthquake engineering, Beijing, China, October

Ruiz S, Madariaga R, Astroza M, Saragoni GR, Lancieri M, Vigny C, Campos J (2012) ort-period rupture process of the 2010 M_w 8.8 Maule earthquake in Chile. Earthq Spectra 28(S1):S1–S18. doi:10.1193/1.4000039

Ruiz S, Metois M, Fuenzalida A, Ruiz J, Leyton F, Grandin R, Vigny C, Madariaga R, Campos J (2014) Intense foreshocks and a slow slip event preceded the 2014 Iquique M_w 8.1 earthquake. Science 345(6201):1165–1169. doi:10.1126/science.1256074

Ruiz S, Klein E, del Campo F, Rivera E, Poli P, Metois M, Christophe V, Baez JC, Vargas G, Leyton F, Madariaga R, Fleitout L (2016) The seismic sequence of the 16 Illapel, Chile, earthquake. Seismol Res Lett. doi:10.1785/0220150281

Scherbaum F, Cotton F, Smit P (2004) On the use of response spectral-reference data for the selection and ranking of ground-motion models for seismic-hazard analysis in regions of moderate seismicity: the case of rock motion. Bull Seismol Soc Am 94(6):2164–2185. doi:10.1785/0120030147

Schurr B, Asch G, Hainzl S, Bedford J, Hoechner A, Palo M, Wang R, Moreno M, Bartsch M, Zhang Y, Oncken O, Tilmann F, Dahm T, Victor P, Barrientos S, Vilotte J-P (2014) Gradual unlocking of plate boundary controlled initiation of the 2014 Iquique earthquake. Nature 512(7514):299–302. doi:10.1038/nature13681

Skarlatoudis AA, Papazachos CB, Margaris BN, Ventouzi C, Kalogeras I, EGELADOS Group (2013) Ground-motion prediction equations of intermediate-depth earthquakes in the Hellenic arc, southern Aegean subduction area. Bull Seismol Soc Am 103(3):1952–1968. doi:10.1785/0120120265

Stewart JP, Douglas J, Javanbarg M, Bozorgnia Y, Abrahamson NA, Boore DM, Campbell KW, Delavaud E, Erdik M, Stafford PJ (2015) Selection of ground motion prediction equations for the global earthquake model. Earthq Spectra 31(1):19–45. doi:10.1193/013013EQS017M

Vigny C, Socquet A, Peyrat S, Ruegg C, Métois M, Madariaga R, Morvan S, Lancieri M, Lacassin R, Campos J, Carrizo D, Bejar-Pizarro M, Barrientos S, Armijo R, Aranda C, Valderas-Bermejo M-C, Ortega I, Bondoux F, Baize S, Lyon-Caen H, Pavez A, Vilotte JP, Bevis M, Brooks B, Smalley R, Parra H, Baez J-C, Blanco M, Cimbaro S, Kendrick E (2011) The 2010 M_w 8.8 Maule Megathrust earthquake of Central Chile, monitored by GPS. Science 332(6036):1417–1421. doi:10.1126/science.1204132

Youngs RR, Chiou S-J, Silva WJ, Humphrey JR (1997) Strong ground motion attenuation relationships for subduction zone earthquakes. Seismol Res Lett 68(1):58–73. doi:10.1785/gssrl.68.1.58

Zhao JX, Irikura K, Zhang J, Fukushima Y, Somerville PG, Asano A, Ohno Y, Oouchi T, Takahashi T, Ogawa H (2006a) An empirical site-classification method for strong-motion stations in Japan using H/V response spectral ratio. Bull Seismol Soc Am 96(3):914–925

Zhao JX, Zhang J, Asano A, Ohno Y, Oouchi T, Takahashi T, Ogawa H, Irikura K, Thio HK, Somerville PG, Fukushima Y, Fukushima Y (2006b) Attenuation relations of strong ground motion in Japan using site classification based on predominant period. Bull Seismol Soc Am 96(3):898–913. doi:10.1785/0120050122